

Supporting Information

Conductive Fibres Constructed on Fully Self-Healable Elastomer Fibres via an Electrospinning Approach

*Jean-Sébastien Bénas^a, Fang-Cheng Liang^a, Yung-Chi Hsu^a, Chun-Hsien Ou^a, Sheng-Yun Chen^a,
Li-Chen Mu^a, Wen-Ya Lee^b, Yu-Chen Chen^c, Wei-Ren Liu^{c,*}, Salahuddin Ahmed^d, Tao Zhou^{d,e,*},
and Chi-Ching Kuo^{a,f,*}*

^a Institute of Organic and Polymeric Materials, National Taipei University of Technology, Taipei 10608, Taiwan

^b Department of Chemical Engineering and Biotechnology, National Taipei University of Technology, Taipei, 10608, Taiwan

^c Department of Chemical Engineering, Chung Yuan Christian University, R&D Center for Membrane Technology, Taoyuan City, 32023, Taiwan

^d Department of Biomedical Engineering, The Pennsylvania State University, PA 16802, USA

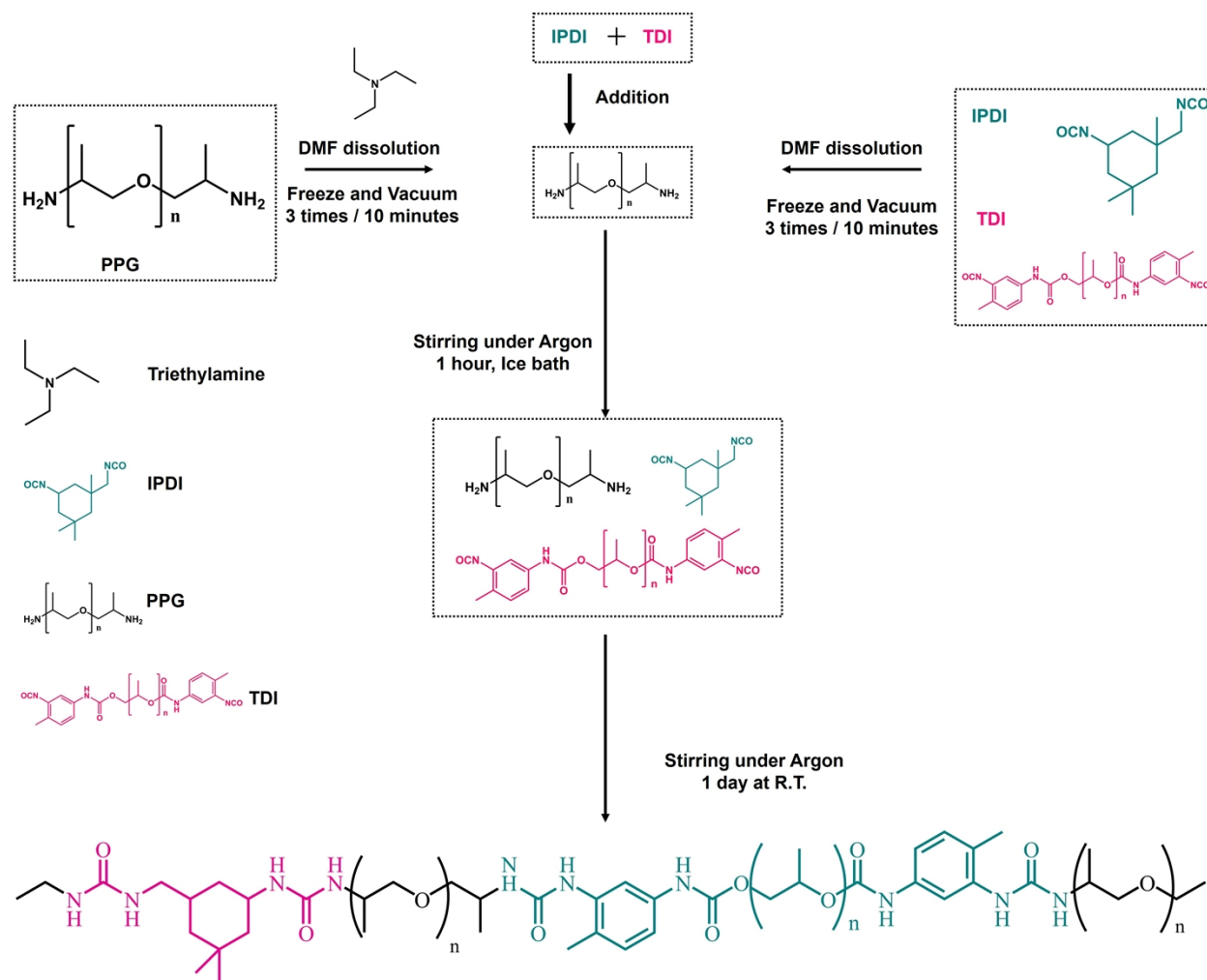
^e Department of Engineering Science and Mechanics, Center for Neural Engineering, The Pennsylvania State University, PA 16802, USA

^f Advanced Research Center for Green Materials Science and Technology, National Taiwan University, Taipei 10617, Taiwan

*Author to whom all correspondence should be addressed

Tel.: 886-2-27712171*2407; Fax: 886-2-27317174

Correspondence to: Prof. C.-C. Kuo (E-mail: kuocc@mail.ntut.edu.tw), Prof. T. Zhou (E-mail: tzz5199@psu.edu), Prof. W.-R. Liu (E-mail: WRLiu1203@gmail.com)



Schematic 1: Building blocks and reaction pathways of PPG-TDI-IPDI self-healing polymer. PPG on one hand and TDI, IPDI building block on the other hand are dissolved in DMF. Then, IPDI and TDI block are added into PPG block to undergo polymerization through urea linker formation for one day. On the middle left are indicated used building block structure and triethylamine catalyst.

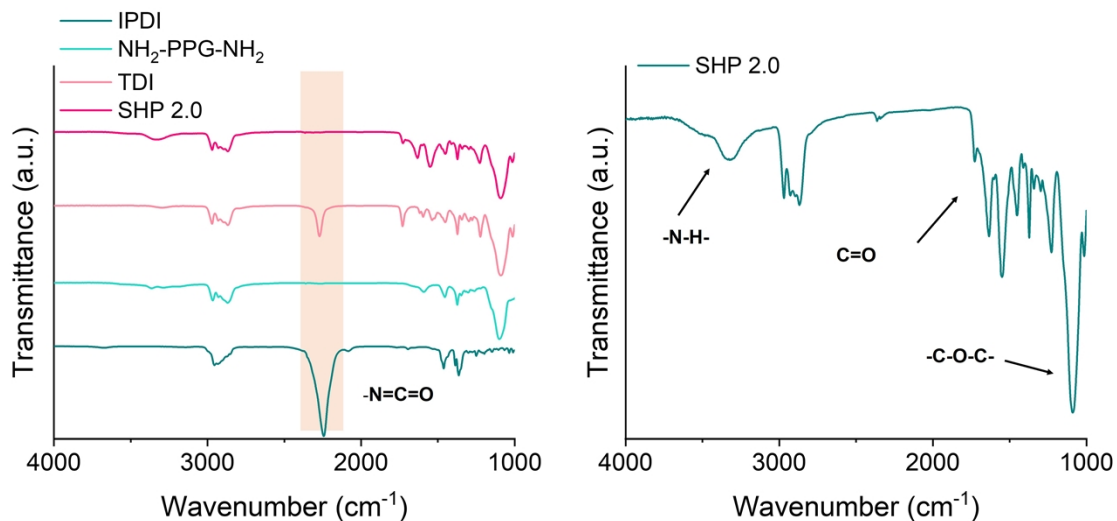


Fig. S1: Self-healing polymer PPG₃-NCO₁-IPDI₂ (SHP 2.0) molecular structure. Left, the isocyanate function (-N=C=O) of TDI and IPDI precursor is indicated. Right, the disappearance of the -N=C=O signal indicate successful reaction with NH₂ end group of PPG building block. The formation of urea linker and crosslinking H-bond is confirmed by the strengthening of the C=O signal at 1630 cm⁻¹.

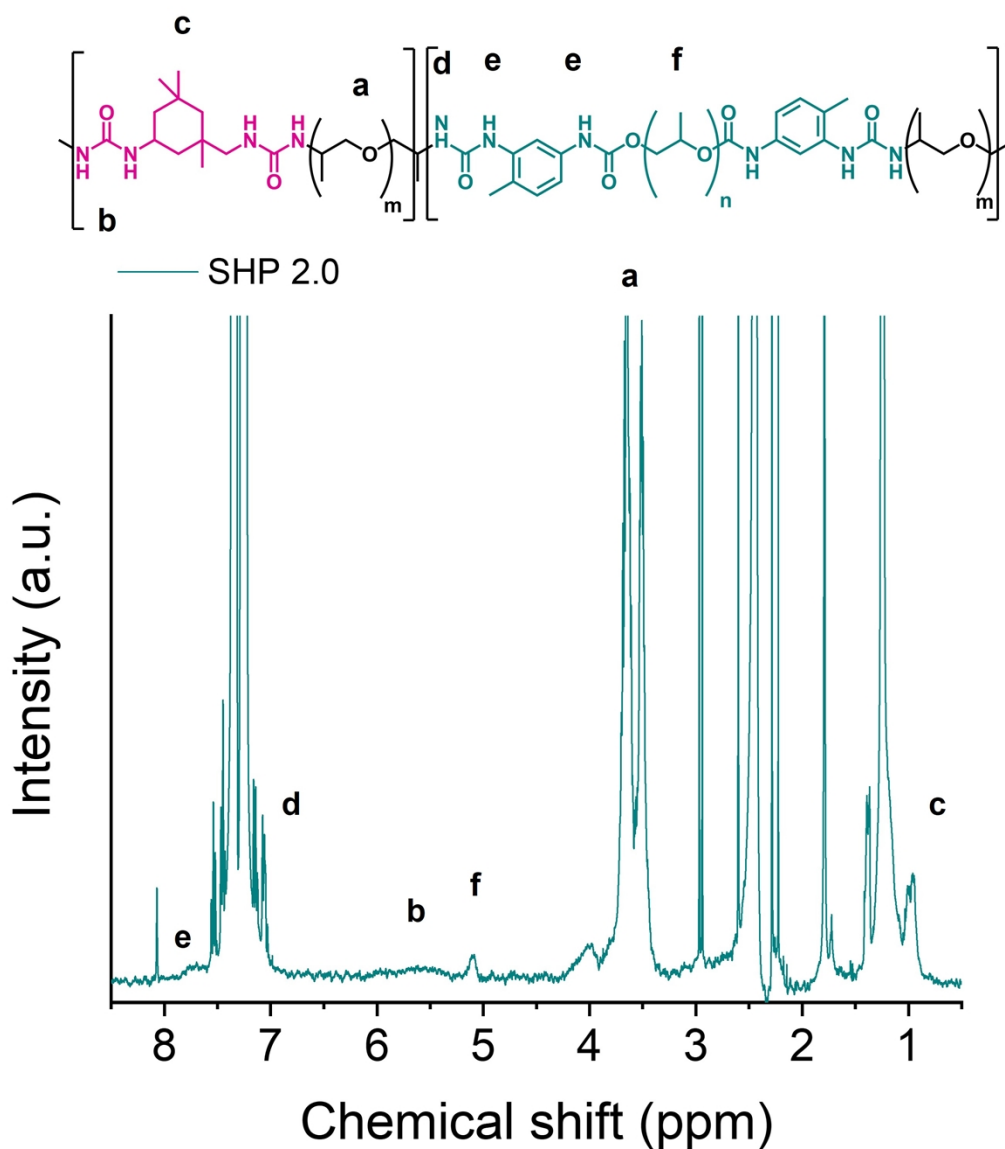


Fig. S2: NMR spectra SHP 2.0 in toluene- d_8 in which each letter indicated correspond to a chemical shift of SHP 2.0 unique function. In details, a (3.70 ppm) corresponds to the PPG segment main backbone. b (5.60 ppm) corresponds to the urea linkage formation of IPDI carbon ring. c (0.85 ppm) corresponds to IPDI carbon rings double methyl substituents. d (7.10 ppm) corresponds to the urea linkage formation of TDI building block. e (7.70 ppm) corresponds to the urethane linkage of TDI building block right to the benzene aromatic ring. f (5.20 ppm) corresponds to the 2-carbon substituted methyl side chain of the PPG (polyol) building block of TDI polyurethane segment.

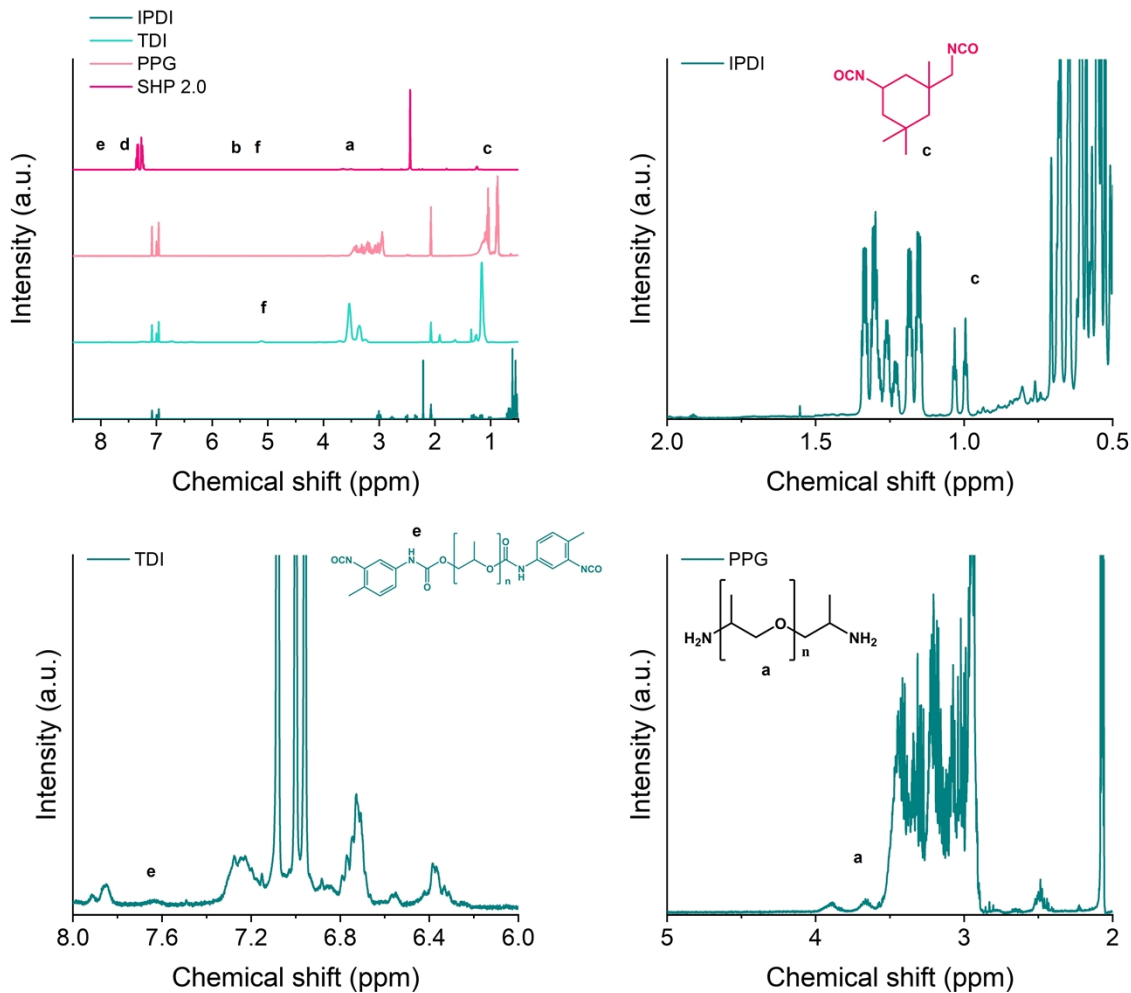


Fig. S3: NMR spectra SHP 2.0 building block in toluene-d₈ and compared with SHP 2.0. In details, on top right c (0.85 ppm) corresponds to IPDI carbon rings double methyl substituents. Bottom left, e (7.70 ppm) corresponds to the urethane linkage of TDI building block right to the benzene aromatic ring. Finally, on bottom right, a (3.70 ppm) corresponds to the PPG segment main backbone.

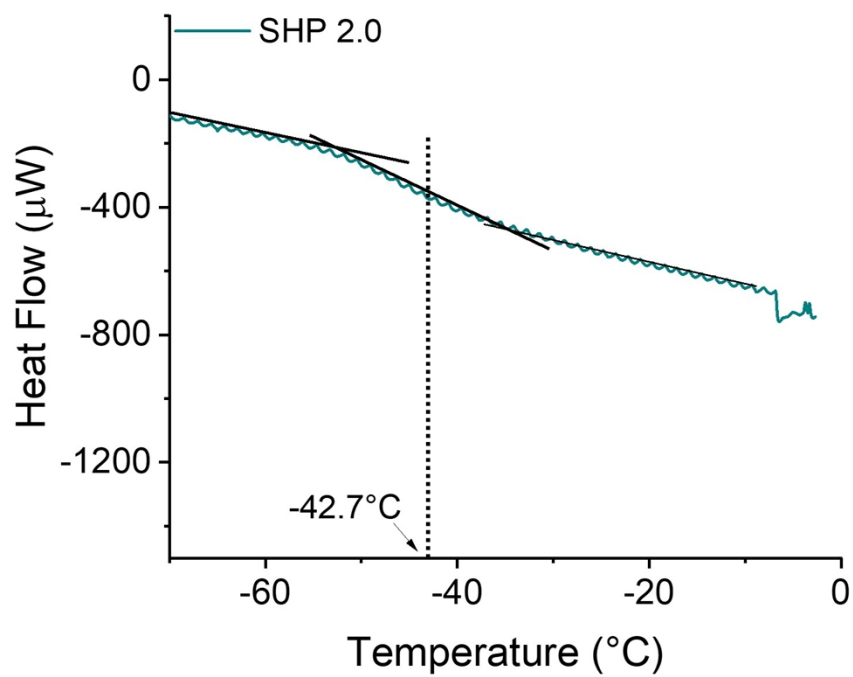


Fig. S4: DSC characterization of SHP 2.0 in which the Tg point is shown at -43°C.

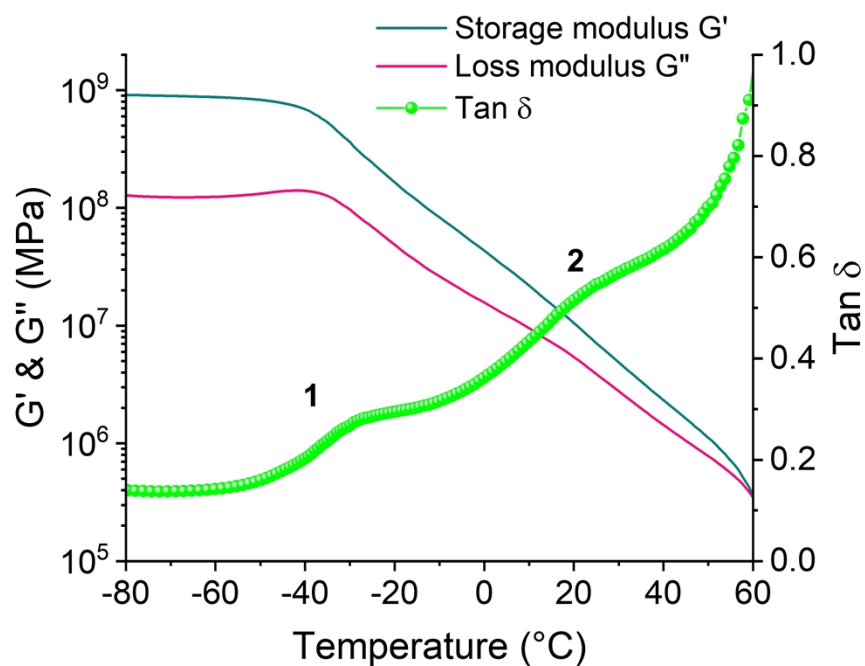


Fig. S5: DMA characterization of SHP 2.0 thin-film at very low strain for temperature ranging from -80 to 60°C. Peak 1 at -35°C and peak 2 at 25°C were characteristic of a partially microphase-separated copolymer and showed the first relaxation of soft segment at freezing temperature followed by relaxation of hard segment at room-temperature.

a

SHP 2.0 (30 wt %) 1:0



b

SHP 2.0 (30 wt %) 7:3

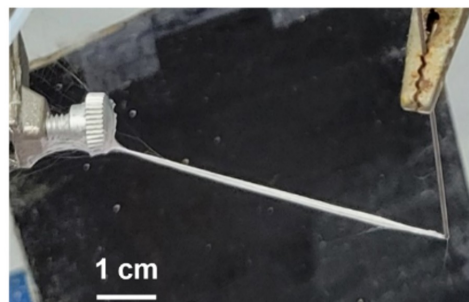


Fig. S6: Influence of the solvent ratio with a fixed SHP ratio for the fabrication of self-healing fibre. a) Pure DCM results in highly elongated SHP 2.0 fibre. b) DCM: results in highly elongated SHP 2.0 fibre with significant optical appearance difference.

SHP 2.0 (30 wt %) 7:3

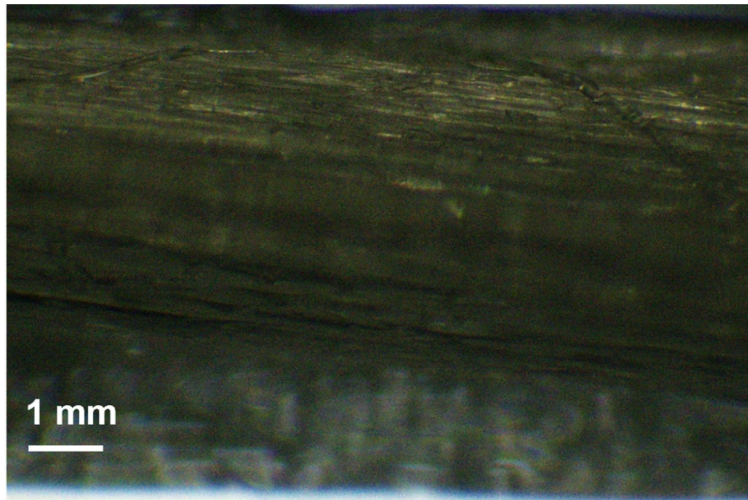
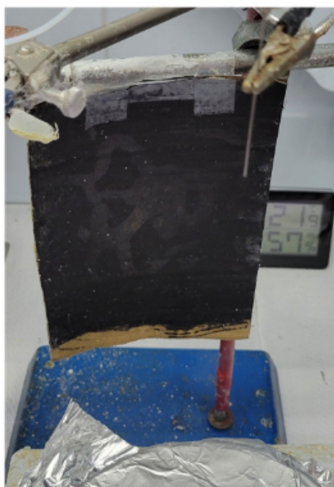


Fig. S7: Optical Microscope image of as-electrospun SHP 2.0 Fibre.

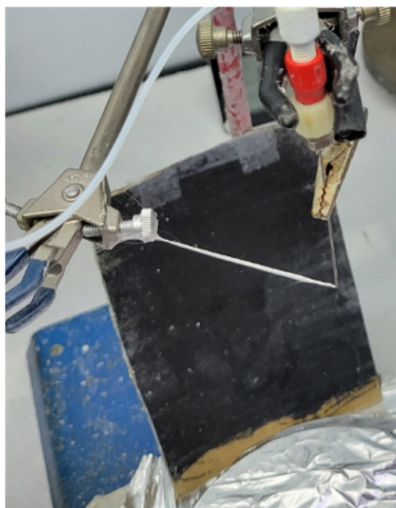
SHP 2.0 (10 wt %) 7:3



SHP 2.0 (20 wt %) 7:3



SHP 2.0 (30 wt %) 7:3



SHP 2.0 (40 wt %) 7:3

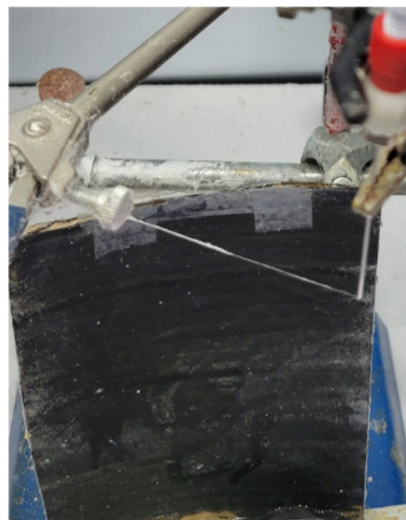


Fig. S8: Influence of the SHP 2.0 weight ratio in a fixed DCM:Ani solution for the fabrication of self-healing fibre. The optimal ratio of SHP 2.0 is 30 wt % in a 7:3 DCM:Ani solution.

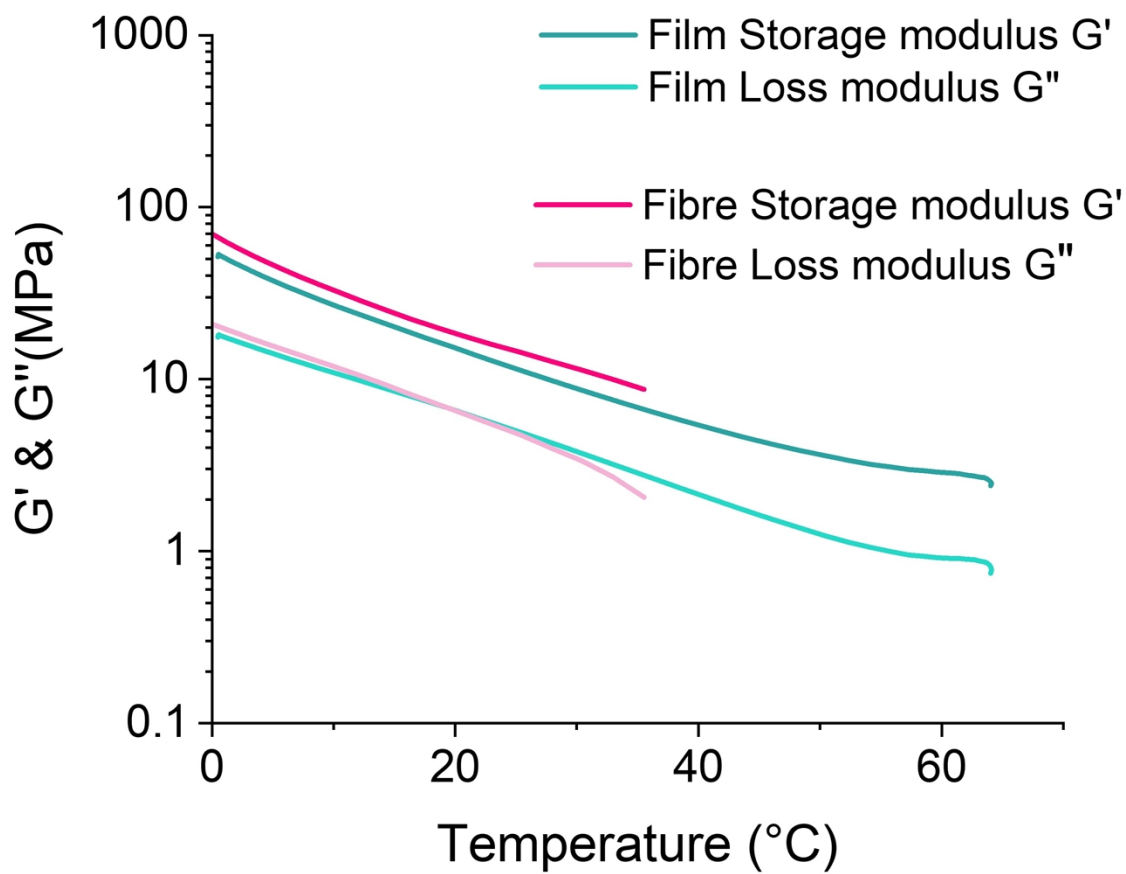


Fig. S9: DMA of SHP 2.0 Thin-Film and Fibre at ambient temperature, only loss and storage modulus are shown in supporting information for clarity.

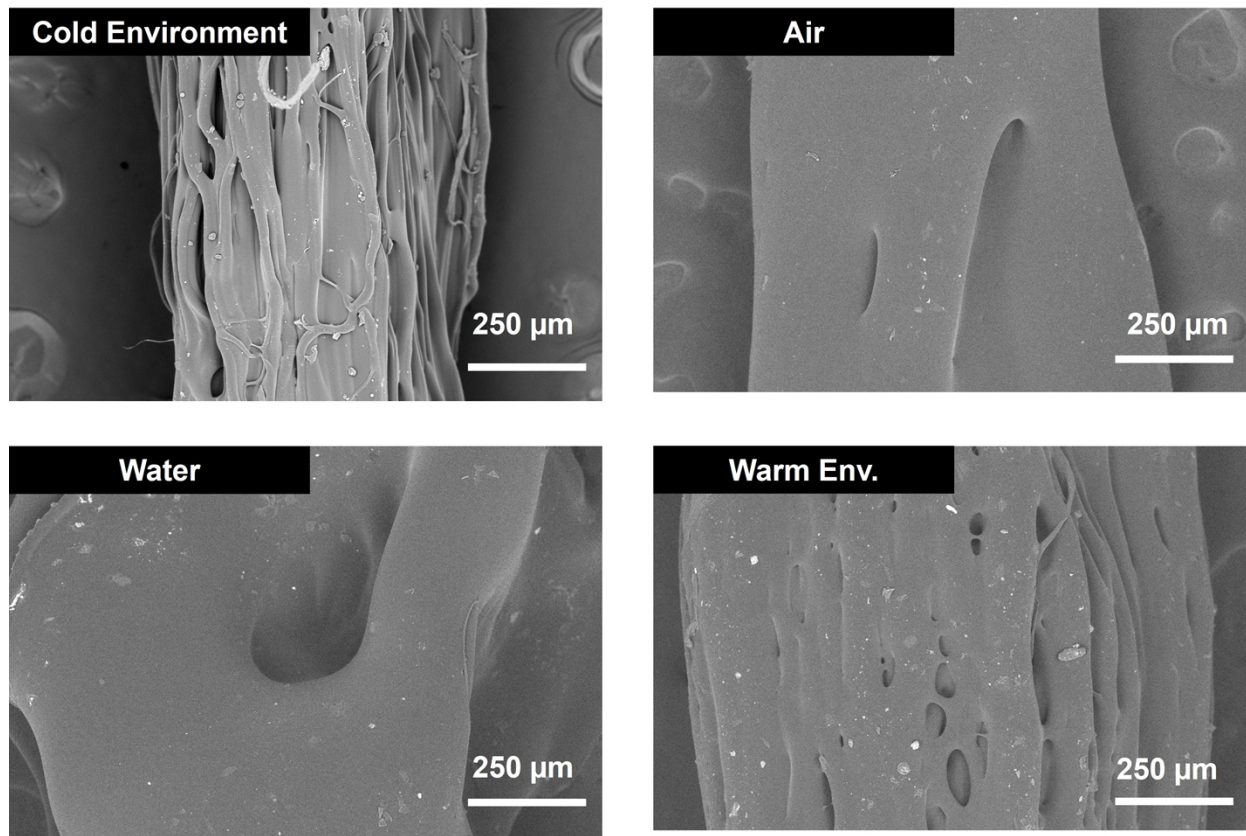


Fig. S10: SHP 2.0 fibre (electrospun with DCM:Ani 7:3) susceptibilities against moisture and air-exposition. In stored cold environment (2°C), SHP 2.0 fibre fibrous structure is sustained while it started to merge upon storage in air after one day. A similar phenomenon is observed when immersed in water or being stored in a warm environment (50°C) after a few hours.

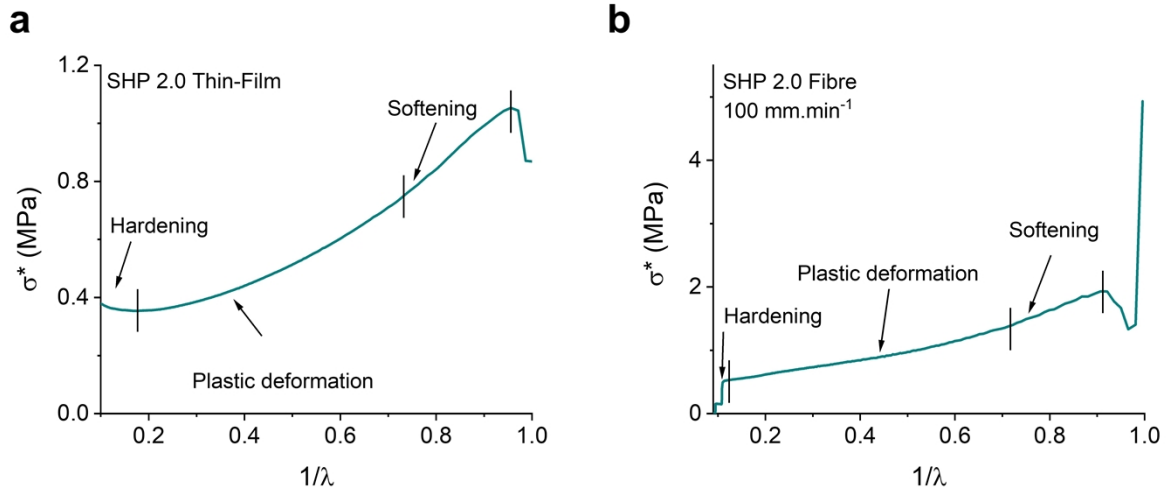


Fig. S11: Mooney-Rivlin representation plot of the SHP 2.0 film and fibre at a strain rate of 100 mm.min⁻¹ and showed SHP 2.0 softening and plastic deformation behavior during stretching in which $\lambda = \varepsilon + 1$ describes the deformation ratio and $\sigma^* = \sigma/(\lambda-\lambda^{-2})$ describe the Mooney stress. For SHP 2.0 thin film, we observed three distinct stages which were the initial force-induced softening ($1/\lambda = 0.955; 0.730$) and transitioning to a long plastic deformation ($1/\lambda = 0.730; 0.170$) and finally SHP hardening ($1/\lambda = 0.170; 0.100$) before breaking. For SHP 2.0 fibre stretched at 100 mm.min⁻¹, the initial force-induced softening ($1/\lambda = 0.907; 0.710$) and transitioning to a long plastic deformation ($1/\lambda = 0.710; 0.120$) and finally SHP hardening ($1/\lambda = 0.120; 0.100$) before breaking.

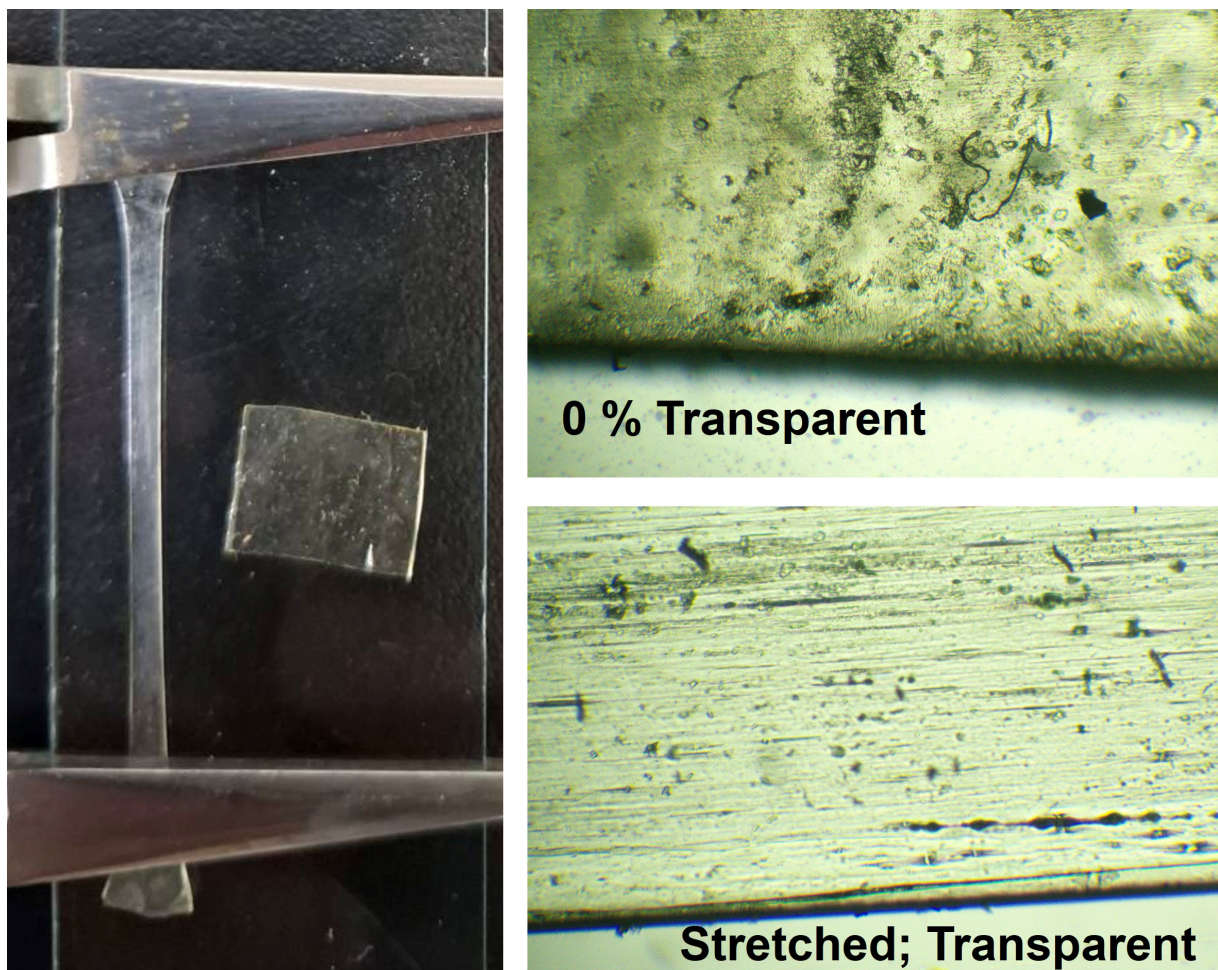


Fig. S12: Comparison of SHP 2.0 thin-film at rest and in a stretched state (left) and optical microscopy observation of SHP 2.0 thin-film is shown on the right in which we observed SHP 2.0 chain alignment alongside stretching direction.

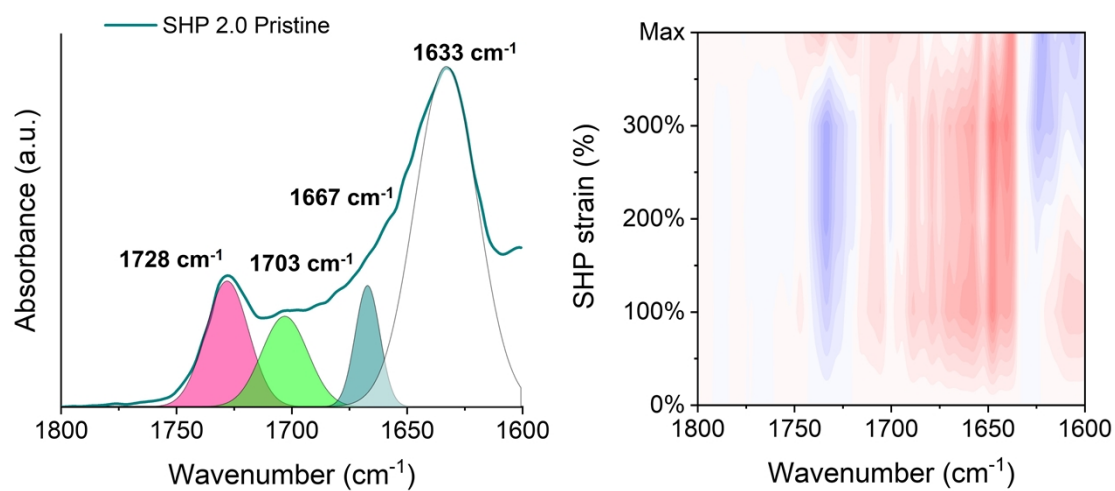


Fig. S13: FTIR analysis of SHP 2.0 thin-film at rest and under strain. The 2D representation of FTIR was plotted using the derivative of absorbance against SHP 2.0 strain with a focus on the Amide I carbonyl signal. Blue region indicates a signal decrease and red region indicate a signal increase relative to the starting point.

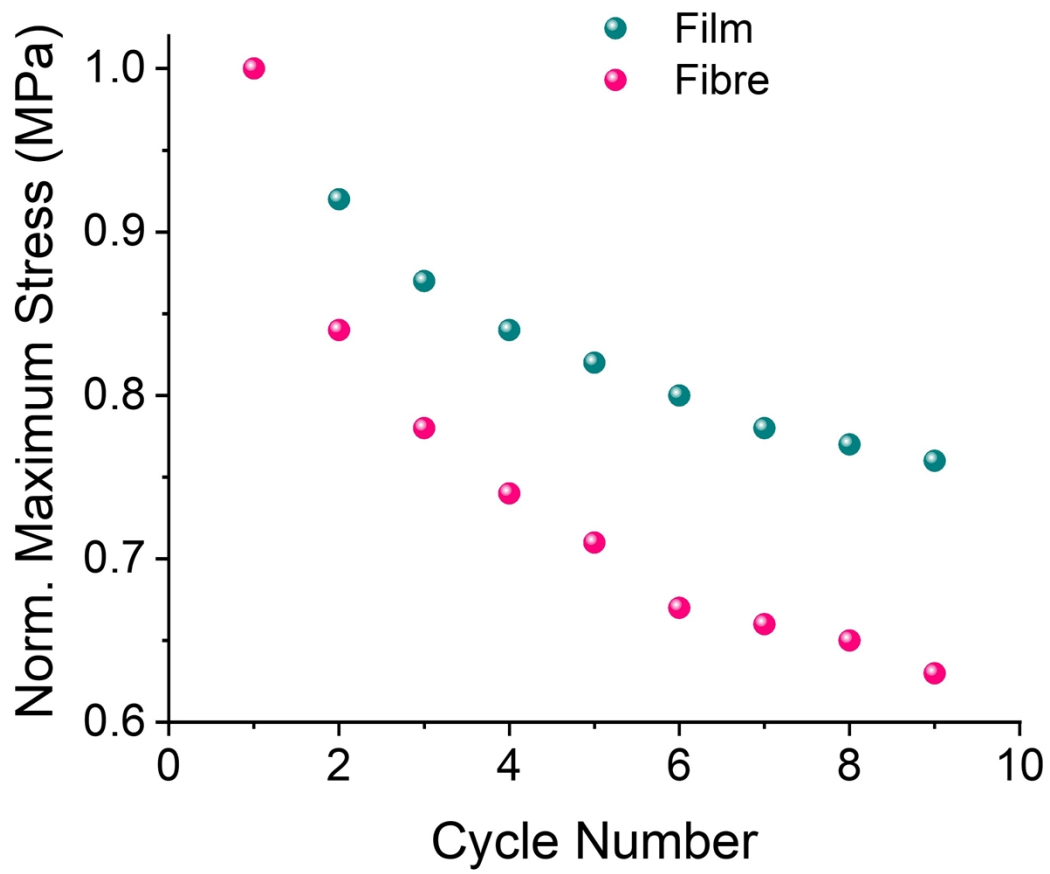


Fig. S14: Evolution of the maximum stress relative to the initial cycle test for both SPH 2.0 thin-film and SHP 2.0 Fibre.

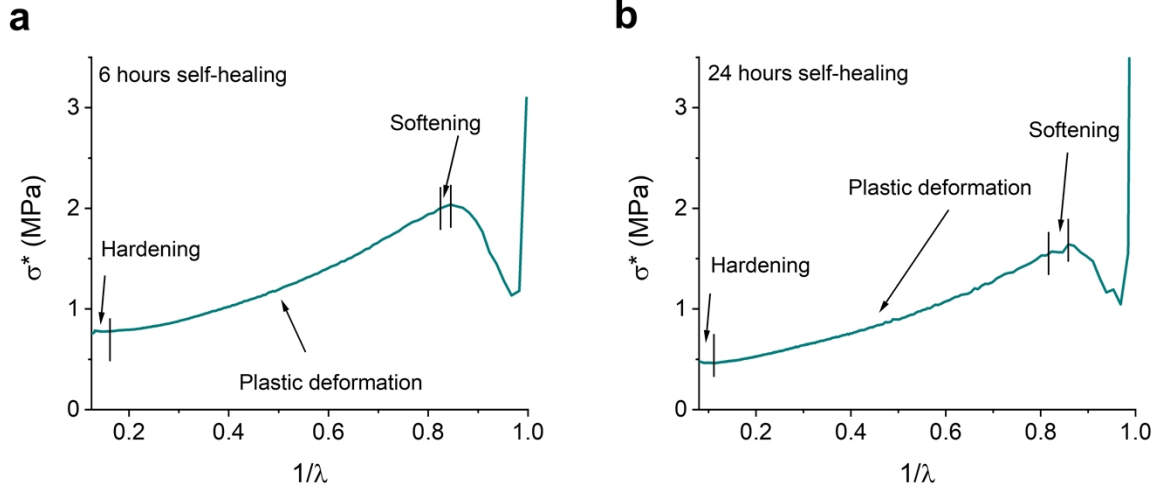


Fig. S15: Mooney-Rivlin representation plot of the SHP 2.0 fibre, following a six and 24 hours cut-repair cycle, at a strain rate of $100 \text{ mm}\cdot\text{min}^{-1}$ and showed SHP 2.0 softening and plastic deformation behavior during stretching in which $\lambda = \epsilon + 1$ describes the deformation ratio and $\sigma^* = \sigma/(\lambda - \lambda^{-2})$ describe the Mooney stress. For SHP 2.0 fibre healed for six hours, we observed three distinct stages which were the initial force-induced softening ($1/\lambda = 0.955; 0.813$) and transitioning to a long plastic deformation ($1/\lambda = 0.813; 0.156$) and finally SHP hardening ($1/\lambda = 0.156; 0.100$) before breaking. For SHP 2.0 fibre healed for 24 hours, the initial force-induced softening ($1/\lambda = 0.907; 0.826$) and transitioning to a long plastic deformation ($1/\lambda = 0.826; 0.110$) and finally SHP hardening ($1/\lambda = 0.120; 0.100$) before breaking.

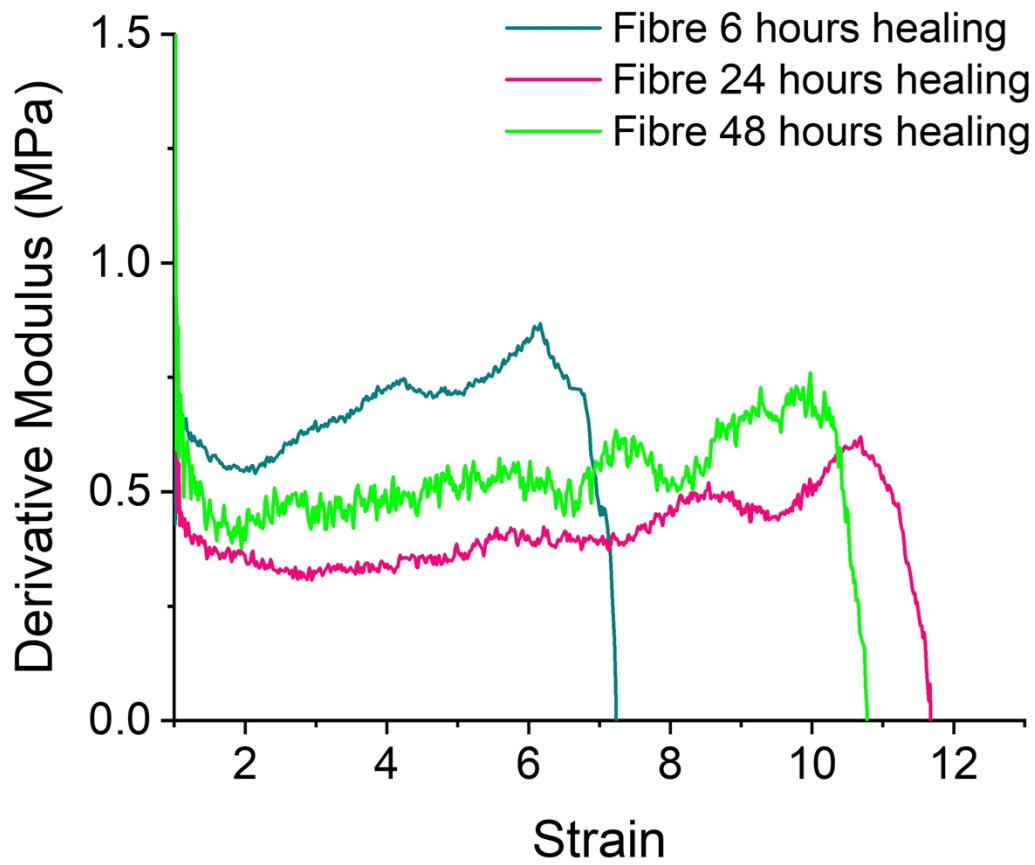


Fig. S16: SHP 2.0 fibre healed at various time variation in tensile modulus versus strain obtained from SHP 2.0 fibre tensile stress-strain curve first derivative.



Fig. S17: SHP 2.0 stretching from a length at rest of 1.2 cm up to a length of 20 cm upon 20 mg weight loading. The circle area indicates the cut-healed area after 12 hours of self-healing process. Further, our fiber, following a 12-hours self-healing process, were attached to a 20 mg weight and stretched up to 1200 % elongating from 1.2 to 20 cm, highlighting remarkable strength.

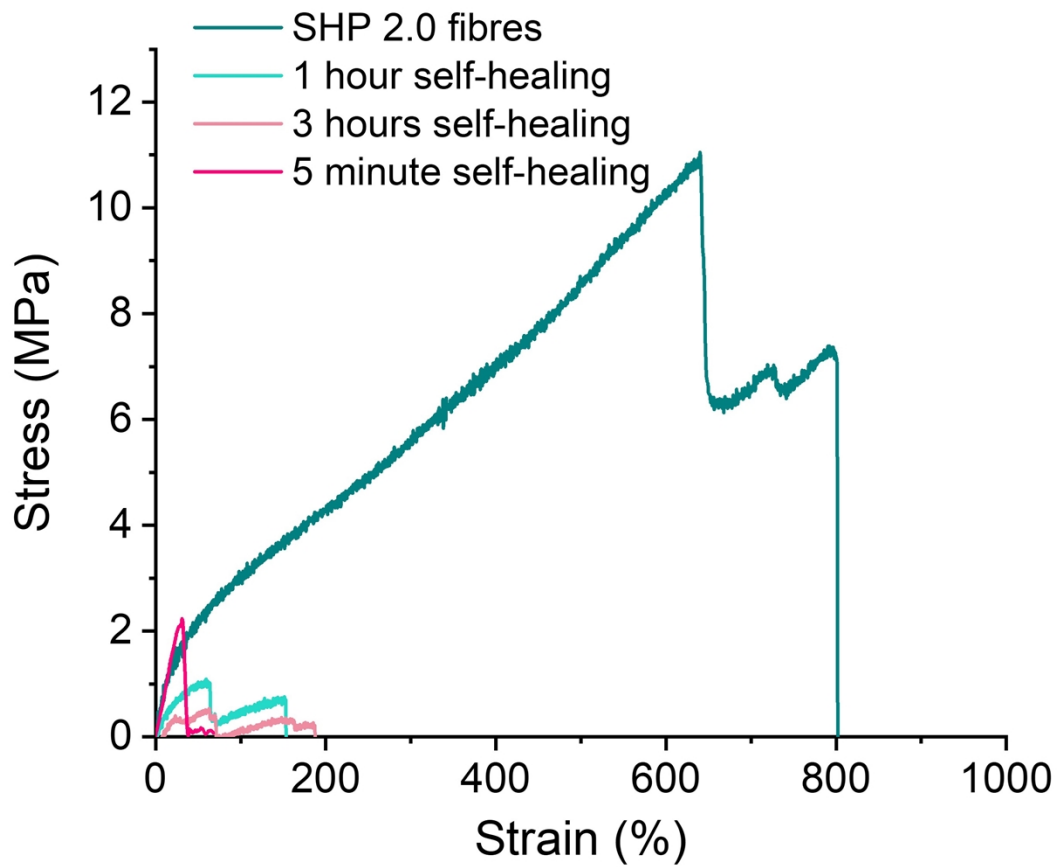


Fig. S18: Tensile stress-strain curve of SHP 2.0 fibre healed at various time from 5 min to 3 hours in air. While we report a 3-hour self-healing time in the main manuscript, we believe that this duration of healing is critical and is a threshold between a clear lack of healing and the beginning of the reconstruction of the H-bond network upon chain flow at the wound interface area.

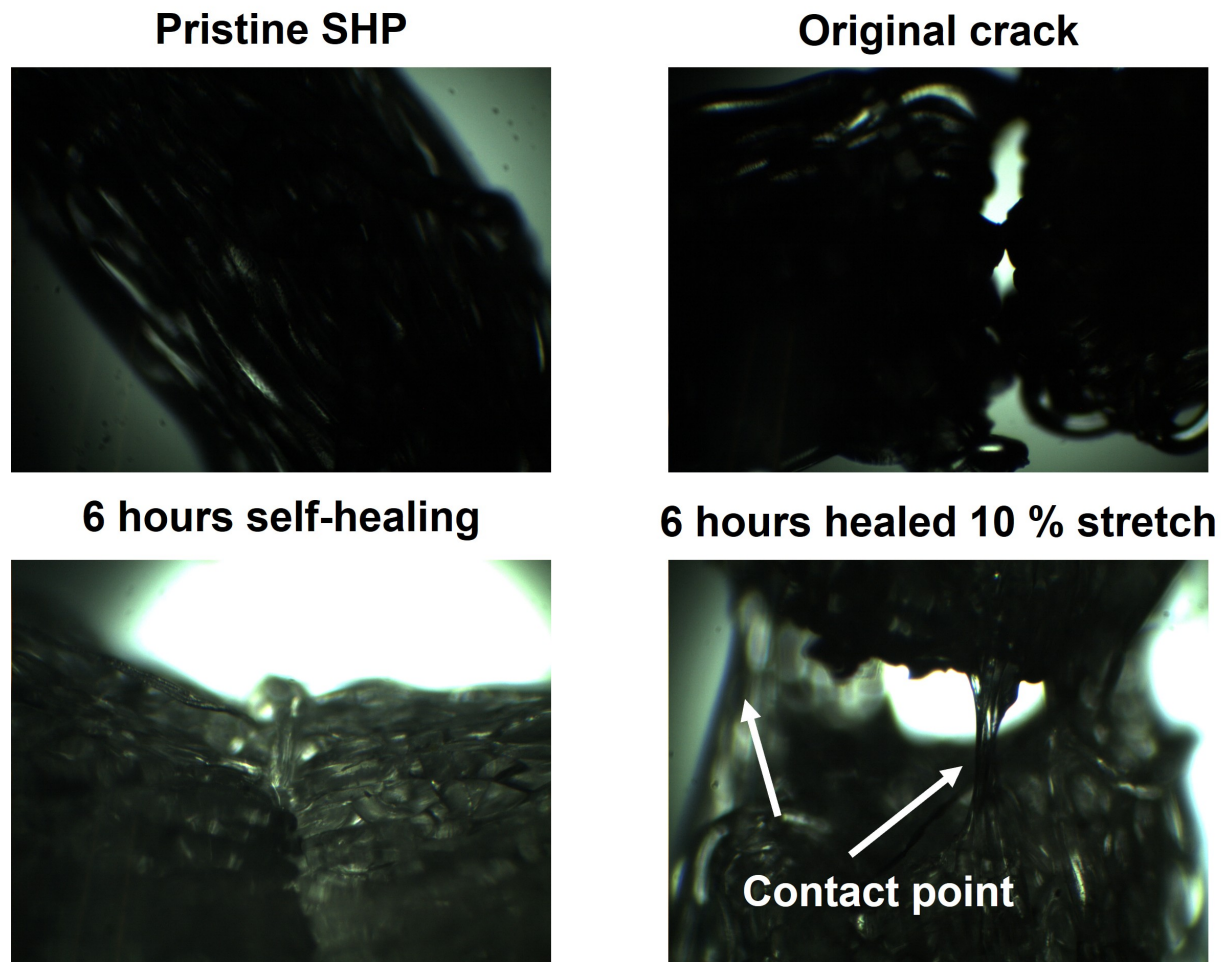


Fig. S19: Optical Microscopy image of SHP 2.0 fibre before and after cut-repair cycle and stretched at 10 % to observe contact point of healing.

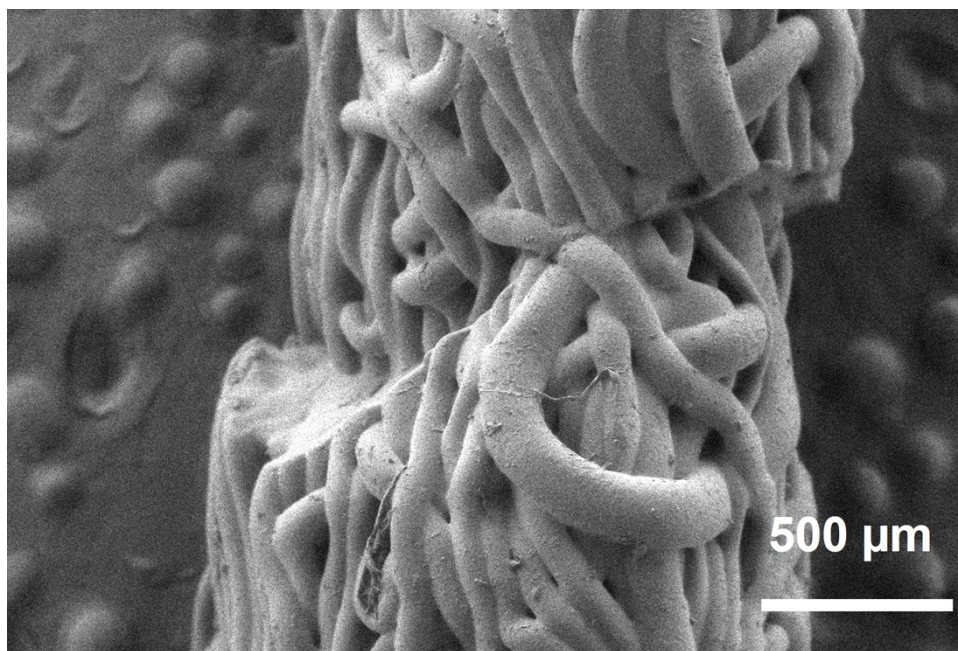


Fig. S20: SEM SHP 2.0 fibre after cut-repair cycle to observe contact point of healing upon improper reconnection of cut fibre at the cut area.

SHP 2.0 Fibre, Synchronous spectra

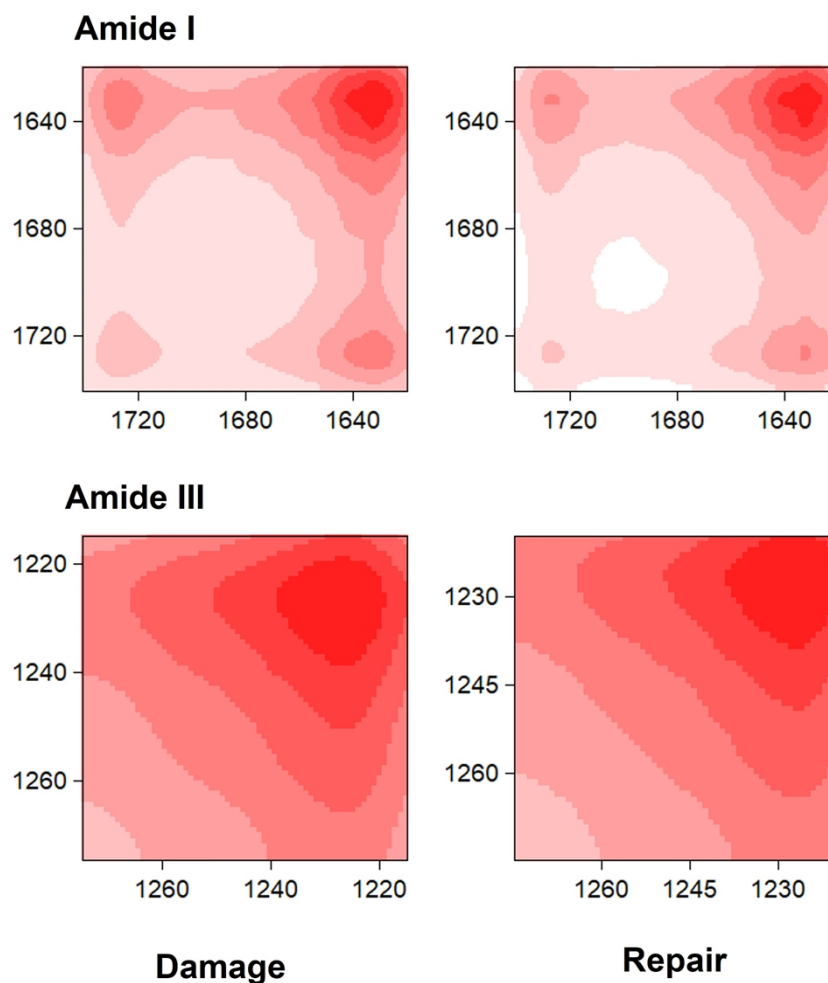


Fig. S21: Synchronous 2D-FTIR spectra of SHP 2.0 fibre of Amide I and Amide III signal, positive peak show correlated behavior but positive cross-peak indicate that H-bond is not the only mechanism at play for SHP 2.0 repair mechanism.

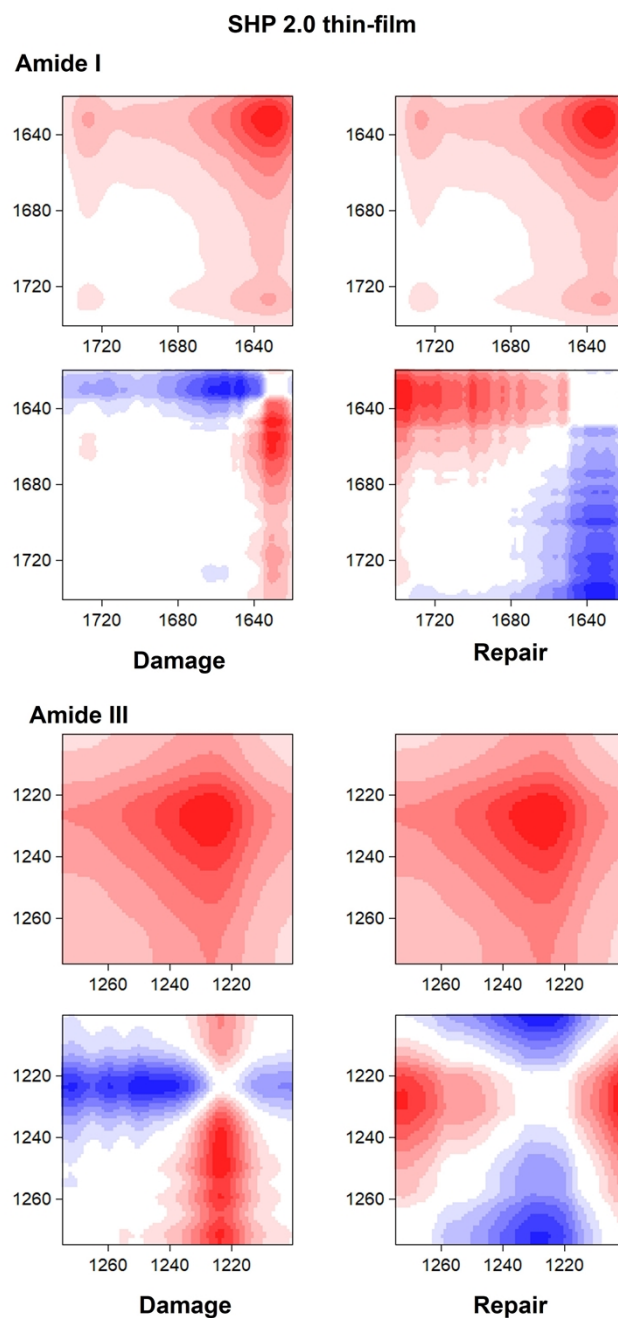


Fig. S22: Synchronous and asynchronous 2D-FTIR spectra of SHP 2.0 thin-film of Amide I and Amide III signal that indicate Amide Free H-bond are formed upon crack but also indicate chain relaxation and conformational change during cut-heal.

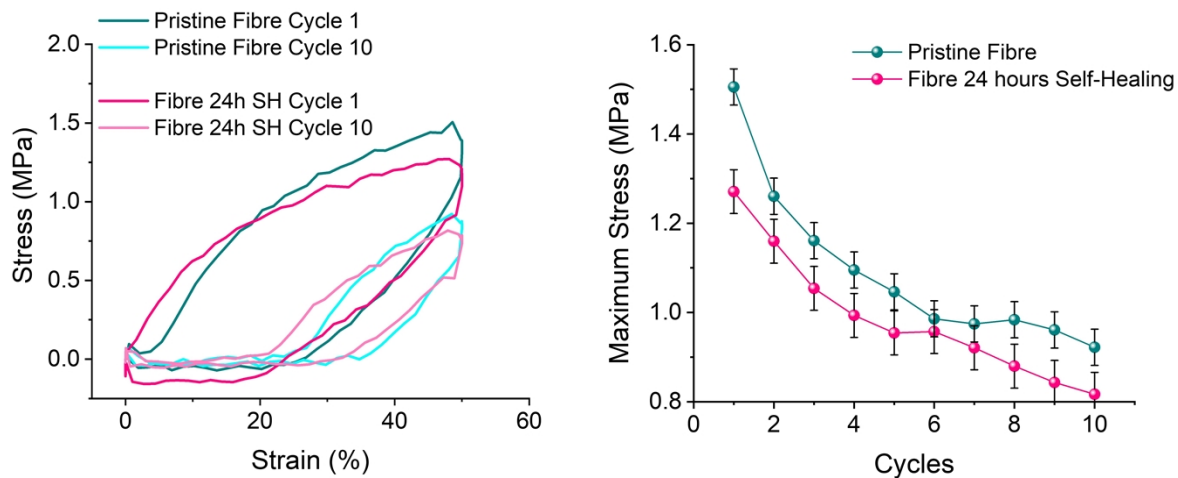


Fig. S23: Cycle Tensile stress-strain curve until 50 % of strain of SHP 2.0 fibre upon 24 hours of self-healing (left) and the evolution of the maximum stress of SHP 2.0 fibres (right).

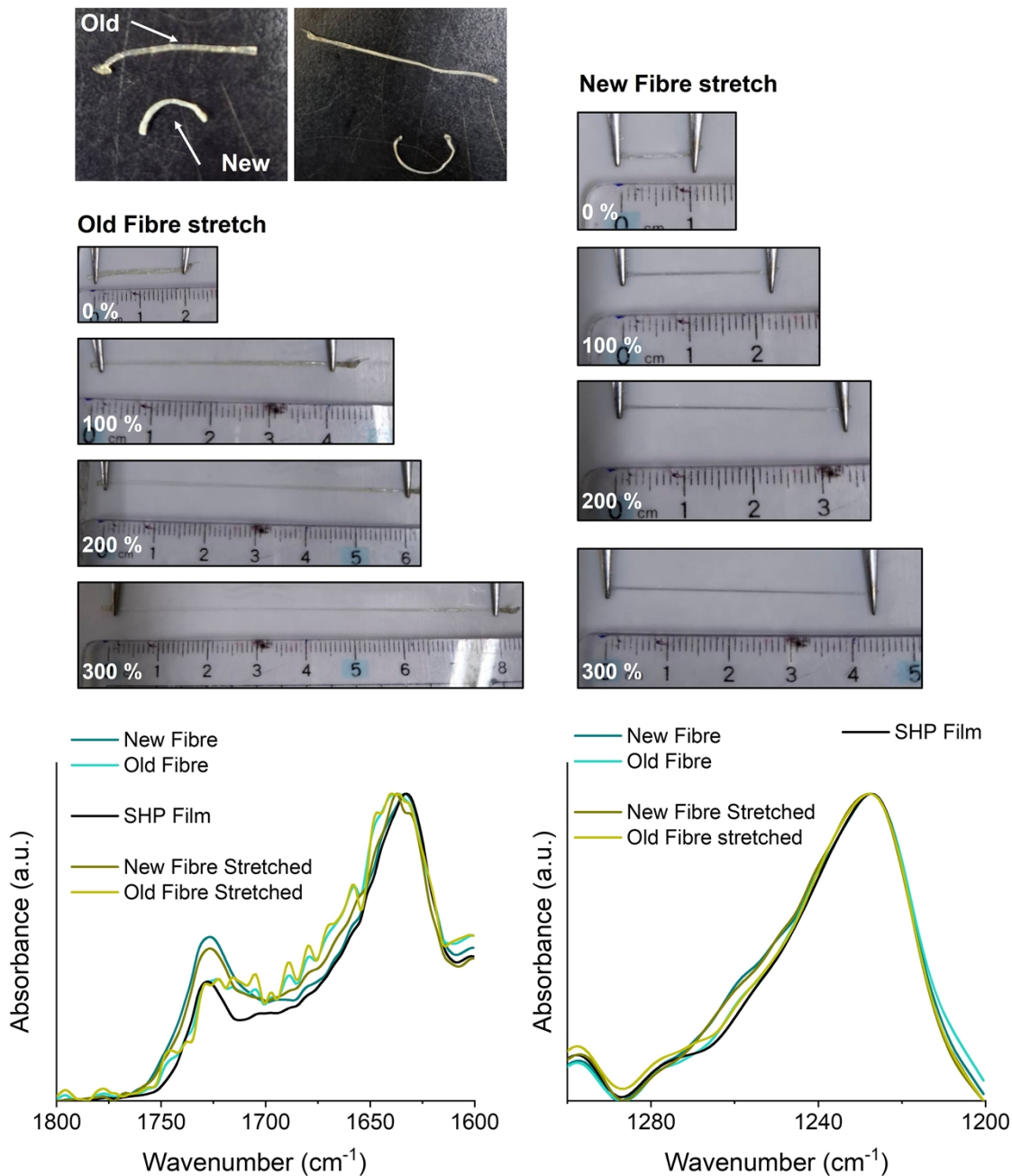


Fig. S24: Top left, comparison of stored SHP 2.0 fibre (old) for several months with freshly fabricated SHP 2.0 fibre before and after stretch. Left, Old fibre were stretched up to 300 % to highlight the disorder-to-order transition of the H-bond arrays. Right, SHP 2.0 fibre were similarly stretched up to 300 % to highlight the disorder-to-order transition of the H-bond arrays. Finally, both their FTIR at rest and stretched was shown for Amide I and III to highlight the H-bond network evolution, SHP film was shown as a visual indication for the reader and indicate the most likely relaxed state of the SHP chain.

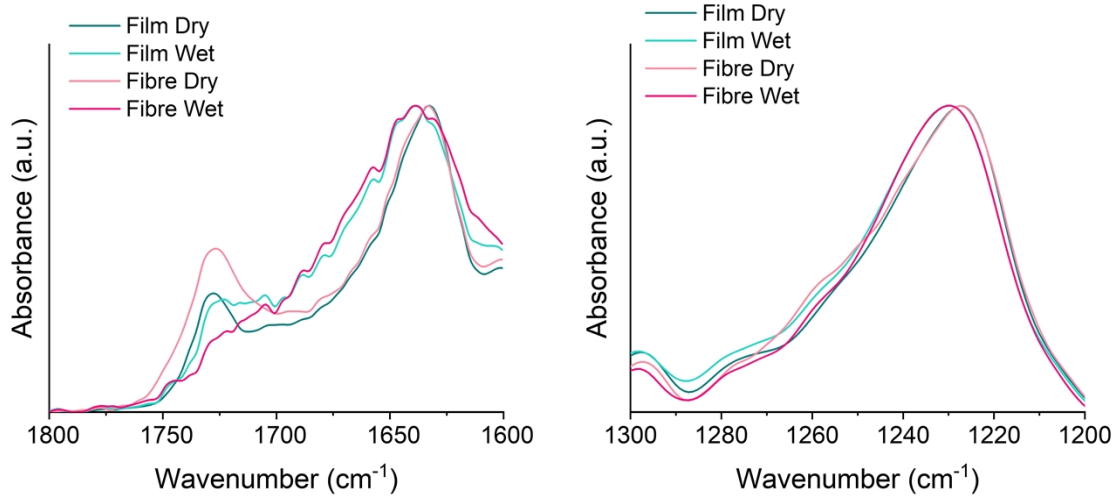


Fig. S25: FTIR spectra of SHP 2.0 fibre dry and wet Amide I (left) and amide III (right) signal.

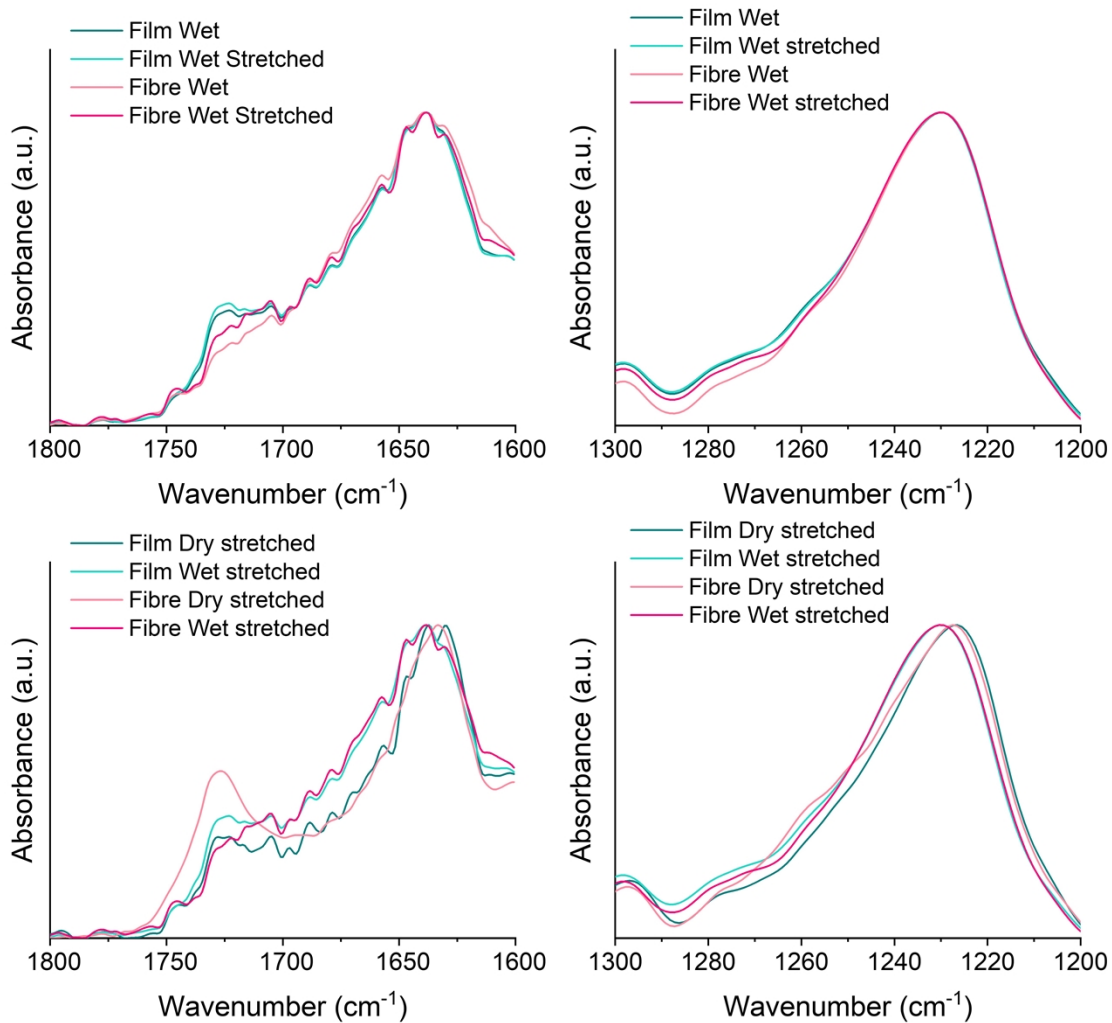


Fig. S26: FTIR spectra of SHP 2.0 fibre wet before and after stretch Amide I (top-left) and amide III (top-right) signal. FTIR spectra of SHP 2.0 fibre dry and wet after stretch Amide I (bottom-left) and amide III (bottom-right) signal.

Wetted SHP 2.0



Dried SHP 2.0



Fig. S27: Photograph of wet and dried SHP 2.0 without external intervention.

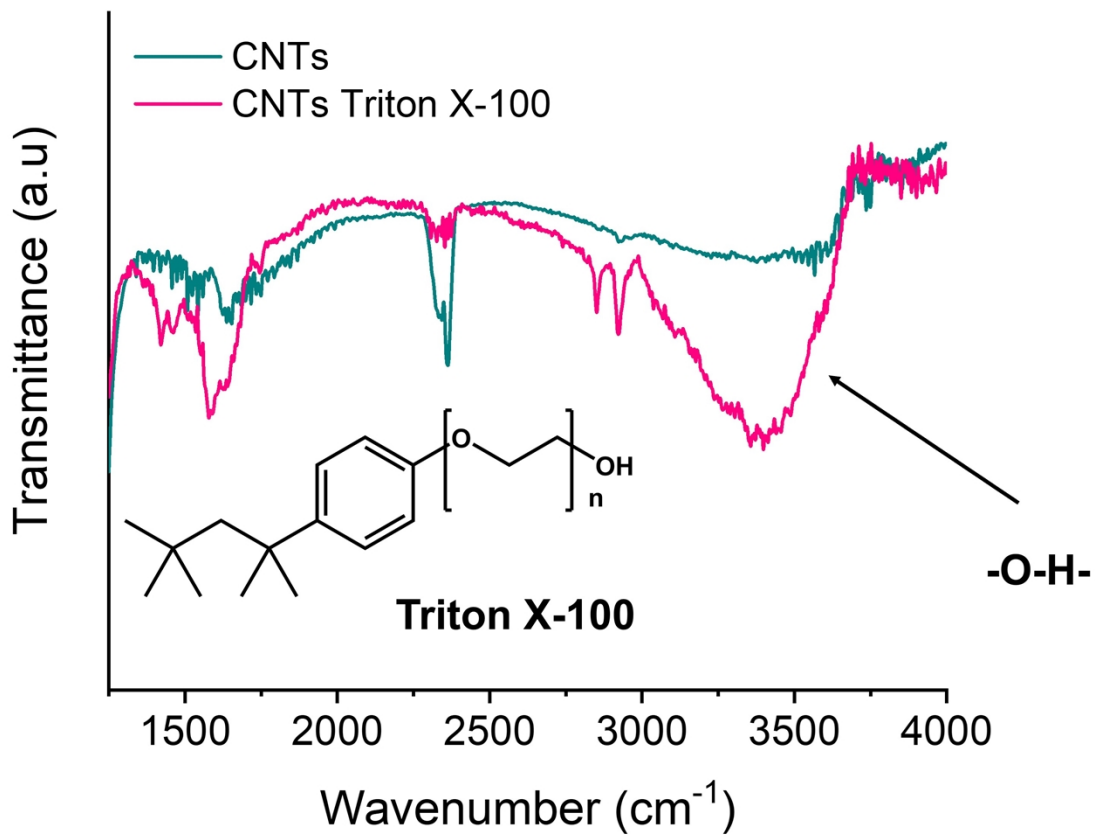


Fig. S28: FTIR characterization to understand Triton X-100 interaction with CNTs.

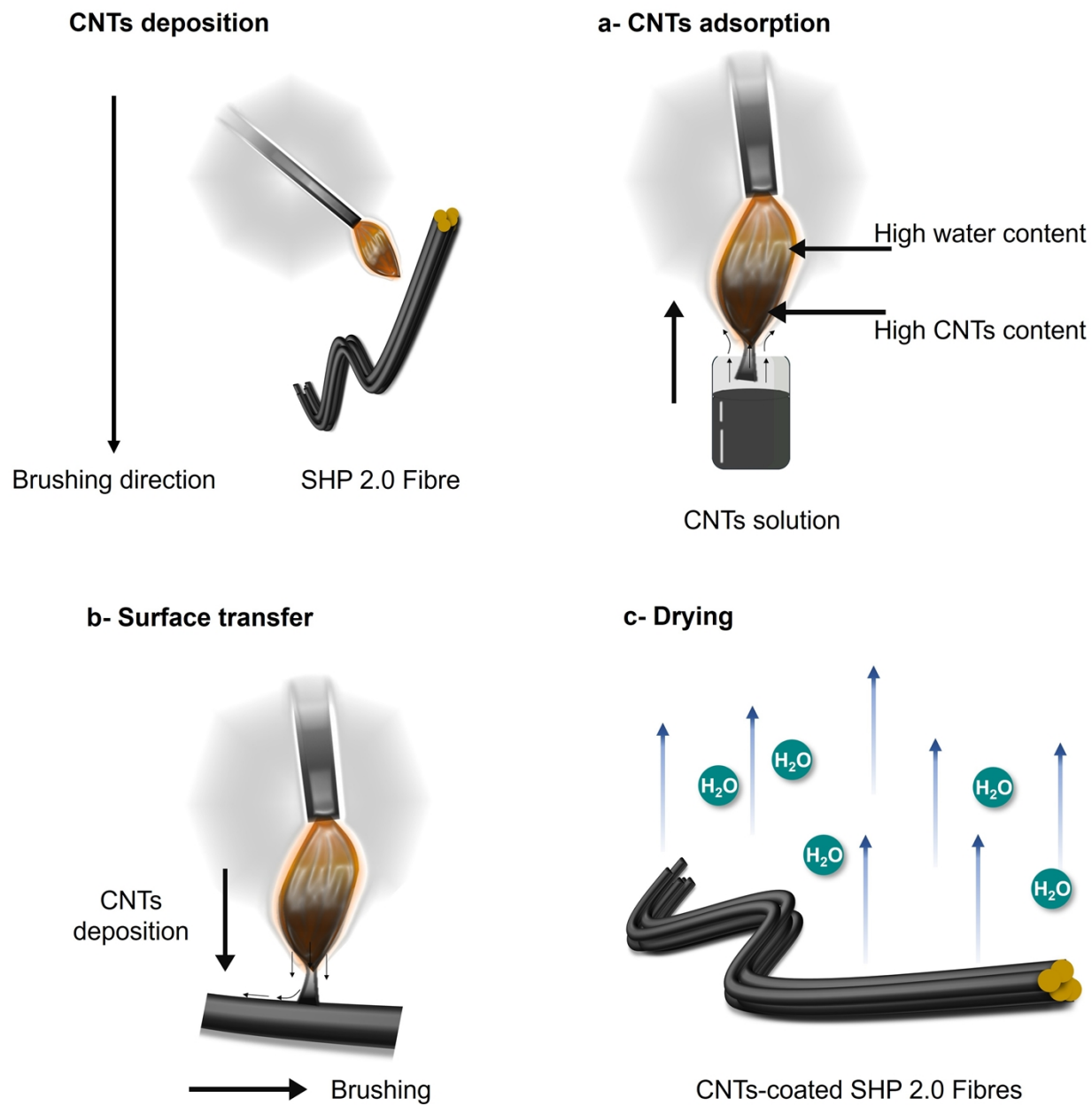


Fig. S29: Brushing of CNTs on top of SHP 2.0 fibre. The method was preferred over dip-coating to minimize as much as possible interaction with water.

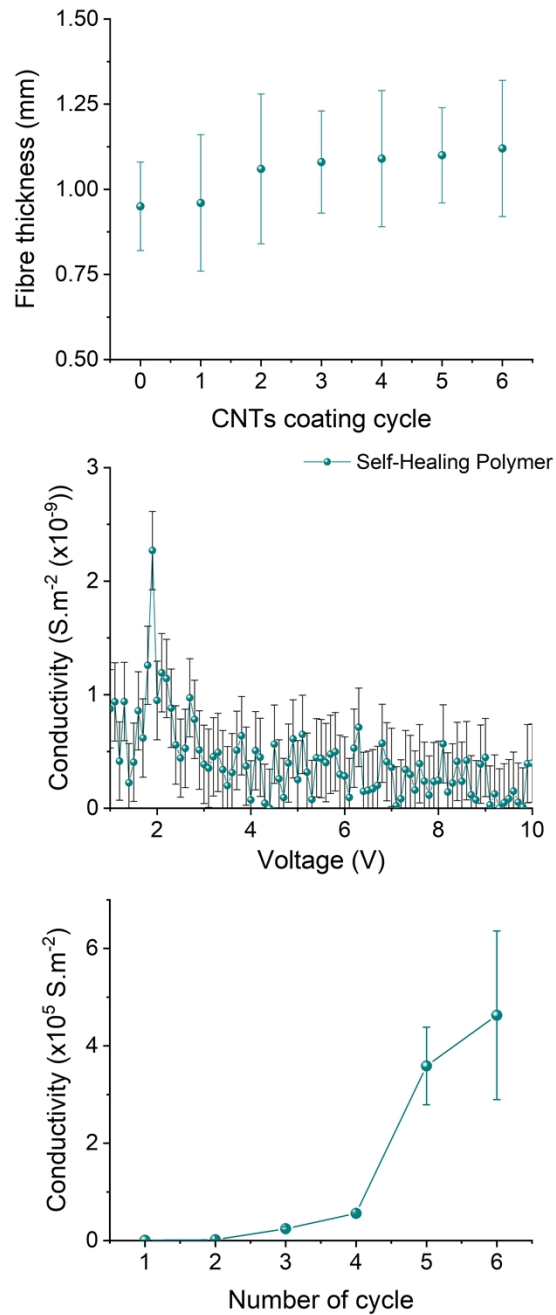


Fig. S30: Evolution of CNTs coating influence onto SHP 2.0 fibre. Top, CNTs thickness increase upon coating considering that one single fibre was used for successive coating. Middle, measure of the pristine SHP 2.0 conductivity without CNTs coating. Right, evolution of SHP 2.0 conductivity following successive coating at 1V.

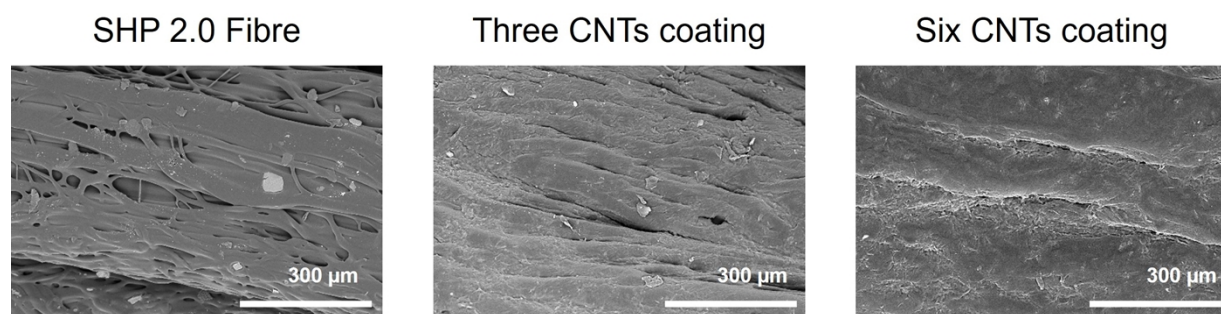
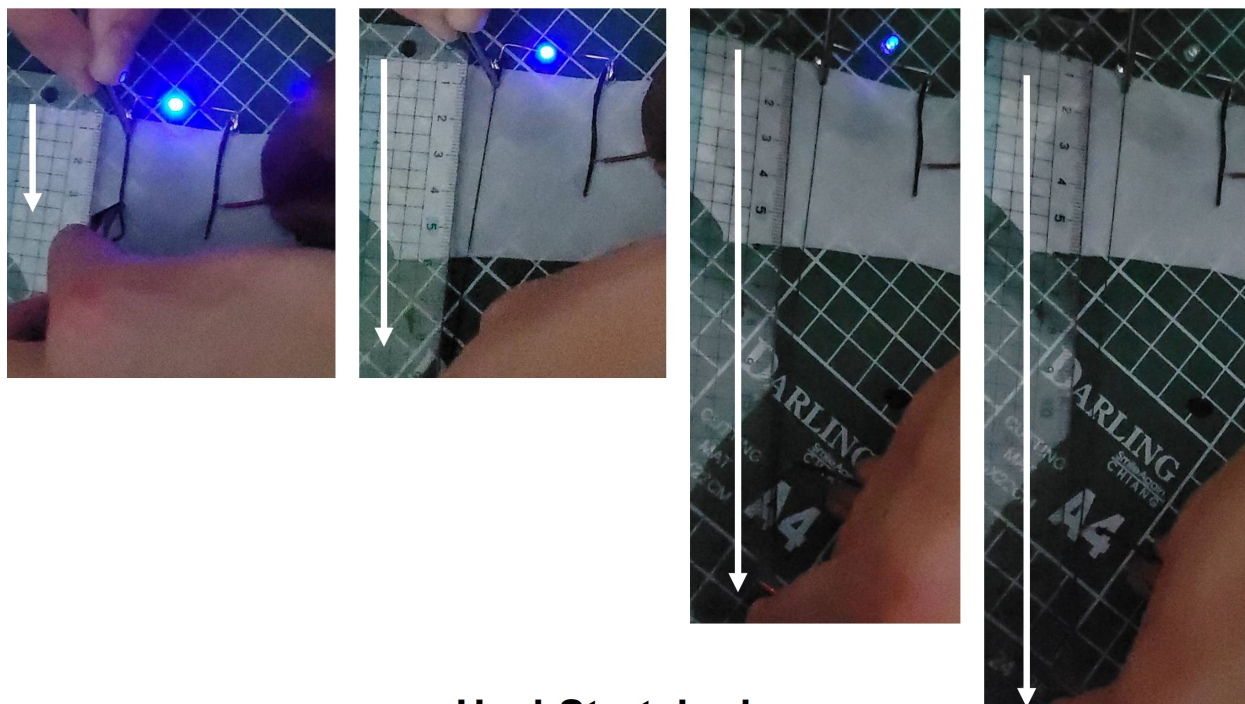


Fig. S31: Evolution of SHP 2.0 Fibre surface morphology before (left), after three-time (middle) and six-time CNTs coating (right).

Stretched



Heal-Stretched

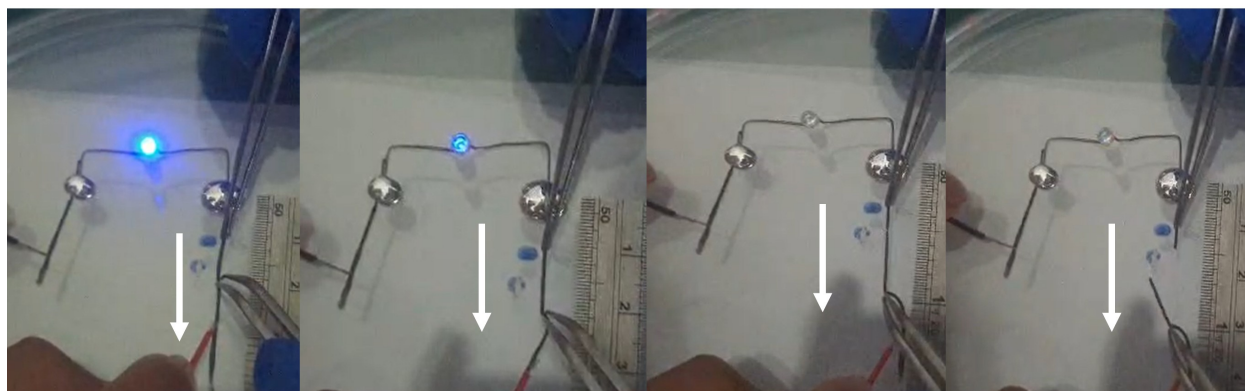


Fig. S32: Top, pristine CNTs-coated SHP 2.0 fibre were stretched until the disappearance of the commercial LEDs blue illumination. Bottom, CNTs-coated SHP 2.0 fibre were cut and reconnected for 10 min before stretching until the disappearance of the commercial LEDs blue illumination, the first part of bottom experiment is shown in the main manuscript **Figure 5**. The white arrow was added as a visual to indicate both SHP 2.0 fibre localization and the stretching direction.

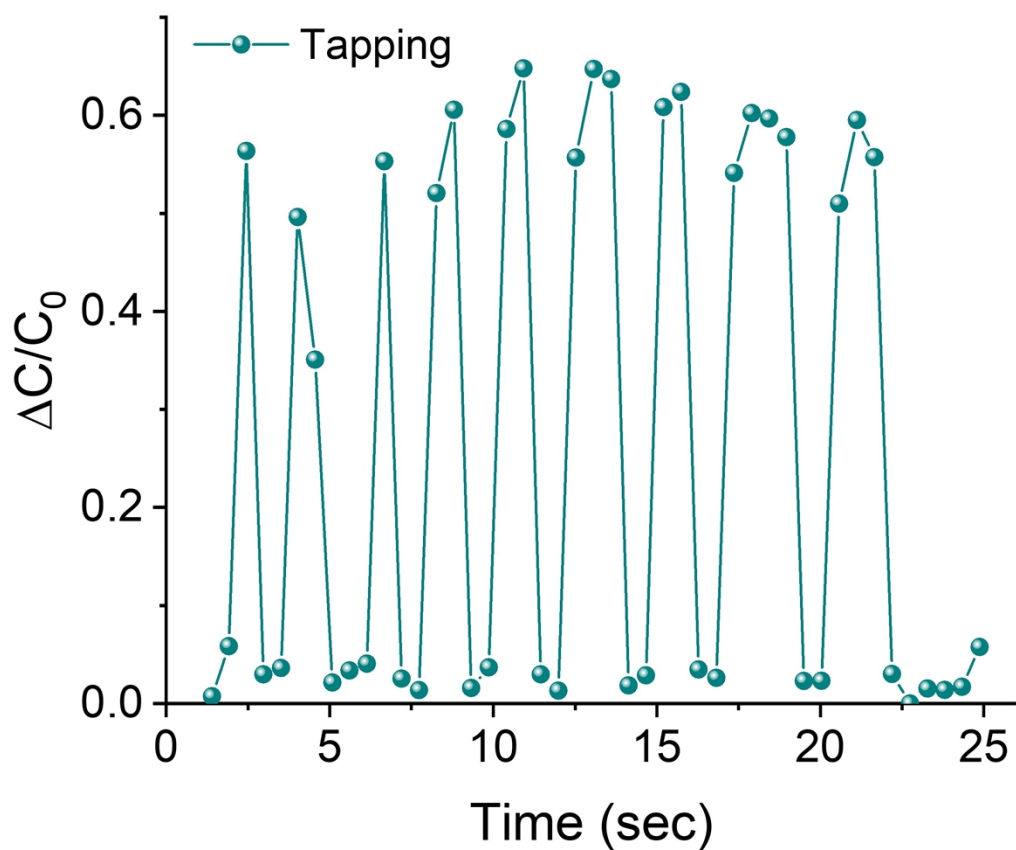


Fig. S33: Finger tapping of the textile-based capacitive sensor device to ensure that our device can properly sense charge gradient at the SHP 2.0 dielectric.

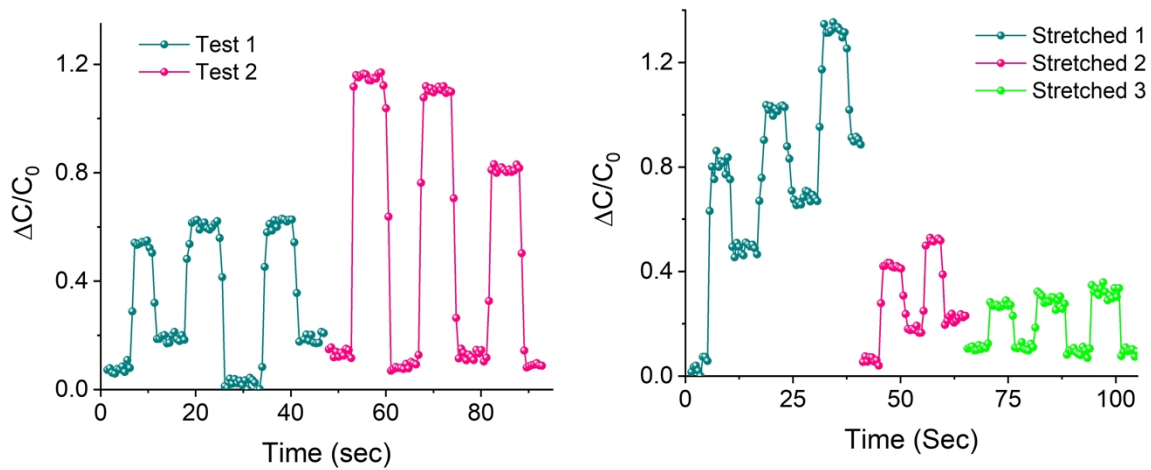


Fig. S34: left, Finger tapping of the textile-based capacitive sensor device with five second cycle. Right, the device was stretched by 50 % and finger tapped with five second cycle.

Table S1: Self-healing polymer film and fiber mechanical characteristics.

Sample	Elongation at break	Stress (MPa)	Fracture Energy (MJ.m ⁻³)
Thin Film	954 ± 4.0 %	4.0 ± 0.4	20 ± 1.0
Fiber 100	811 ± 4.5 %	4.5 ± 0.7	27 ± 1.1
Fiber 200	1133 ± 6.1 %	6.1 ± 0.9	41 ± 1.5
Fiber 500	1236 ± 8.9 %	8.9 ± 1.2	63 ± 2.2
Fiber 1000	773 ± 9.5 %	9.5 ± 1.3	43 ± 2.3

Table S2: Self-healing polymer fiber mechanical characteristics after self-healing.

Sample	Elongation at break	Stress (MPa)	Fracture Energy (MJ.m ⁻³)	Self-healing efficiency
Pristine fibers	811 ± 4.5	4.5 ± 0.7	27 ± 1.1	-
6 h self-healing	728 ± 6.2	6.2 ± 0.9	27 ± 1.5	100 % ± 11
24 h self-healing	1175 ± 5.9	6.0 ± 0.8	40 ± 1.4	148 % ± 11
48 h self-healing	1094 ± 7.6	7.5 ± 1.1	49 ± 1.8	181 % ± 11

Table S3: Comparison of different self-healable fiber-based system with our work.

System	Architecture	Mechanical properties	Self-healing efficiency	Conductivity	Ref.
PAA-AgNWs-PDMS	Conductive fibre	2400 % strain	80 % original strain after 12 hours	1.0×10^6 S.m ⁻¹	1
PDMS-PU coated by bPEI-PAA	Fibrous network	Maximum stress of 467.81 kPa	91.81 % original stress after 6 hours	-	2
PAN-WO ₃ coated by bPEI-PAA	Fibrous network	-	-	-	3
FFS and CFS	Fibrous network	-	Fibers merging observed	-	4
PBA-HDI-IPDH-Liquid Metal	Conductive fibre	Tensile strength of 73 MPa	74 % efficiency after 12 hours at 110°C	9.8×10^4 S.m ⁻¹	5
MP-rGO	Conductive fibre	Stress of 9.3 MPa	Over 80 % self-healing efficiency	120 S.m ⁻¹	6
SHP 2.0 - CNTs	Conductive fibre	Toughness of 45 MJ.m ⁻³	100 % original toughness after 6 hours	1.0×10^5 S.m ⁻¹	This work

References

1. M. Rong, D. Chen, H. Hu, F. Chen, Y. Zhang, C. Xie, Z. Chen, Y. Yu, Y. Xie, H. Yao, Q. Huang and Z. Zheng, *Small*, 2023, **19**, e2304353.
2. M. Zhu, J. Yu, Z. Li and B. Ding, *Angew. Chem. Int. Ed. Engl.*, 2022, **61**, e202208949.
3. W. Ma, Y. Li, S. Gao, J. Cui, Q. Qu, Y. Wang, C. Huang and G. Fu, *ACS Appl. Mater. Interfaces*, 2020, **12**, 23644-23654.
4. S. Choi, Y. Eom, S. M. Kim, D. W. Jeong, J. Han, J. M. Koo, S. Y. Hwang, J. Park and D. X. Oh, *Adv. Mater.*, 2020, **32**, e1907064.
5. S. Wang, Z. Ouyang, S. Geng, Y. Wang, X. Zhao, B. Yuan, X. Zhang, Q. Xu, C. Tang, S. Tang, H. Miao, H. Peng, H. Sun, *Natl. Sci. Rev.*, 2024, **11**, nwae006.
6. P. Niu, N. Bao, H. Zhao, S. Yan, B. Liu, Y. Wu, H. Li, *Compos. Sci. Technol.*, 2022, **219**, 109261.